THE JOURNAL OF BIOLOGICAL CHEMISTRY VOL. 291, NO. 11, pp. 5740–5752, March 11, 2016
Published in the U.S.A.

Large Conformational Changes of Insertion 3 in Human Glycyl-tRNA Synthetase (hGlyRS) during Catalysis*

Received for publication, July 21, 2015, and in revised form, January 4, 2016 Published, JBC Papers in Press, January 21, 2016, DOI 10.1074/jbc.M115.679126

Xiangyu Deng[‡§], Xiangjing Qin[¶], Lei Chen[‡§], Qian Jia[‡§], Yonghui Zhang[‖], Zhiyong Zhang[‖], Dongsheng Lei[**], Gang Ren[**], Zhihong Zhou[‡§], Zhong Wang[§‡‡], Qing Li[§‡‡], and Wei Xie[‡§1]

*From the [‡]State Key Laboratory for Biocontrol, School of Life Sciences, Sun Yat-Sen University, Guangzhou, Guangdong 510275, China, the [§]Center for Cellular and Structural Biology and the [‡‡]School of Pharmaceutical Sciences, Sun Yat-Sen University, University City, Guangzhou, Guangdong 510006, China, the [¶]South China Sea Institute, Chinese Academy of Sciences, Guangzhou, Guangdong 510301, China, the [‖]Hefei National Laboratory for Physical Science at Microscale and School of Life Sciences, University of Science and Technology of China, Hefei, Anhui 230026, China, and the **Molecular Foundry, Lawrence Berkeley National Laboratory, Berkeley, California 94720*

Glycyl-tRNA synthetase (GlyRS) is the enzyme that covalently links glycine to cognate tRNA for translation. It is of great research interest because of its nonconserved quaternary structures, unique species-specific aminoacylation properties, and noncanonical functions in neurological diseases, but none of these is fully understood. We report two crystal structures of human GlyRS variants, in the free form and in complex with $tRNA^{Gly}$ respectively, and reveal new aspects of the glycylation mechanism. We discover that insertion 3 differs considerably in conformation in catalysis and that it acts like a "switch" and fully opens to allow tRNA to bind in a cross-subunit fashion. The flexibility of the protein is supported by molecular dynamics simulation, as well as enzymatic activity assays. The biophysical and biochemical studies suggest that human GlyRS may utilize its flexibility for both the traditional function (regulate tRNA binding) and alternative functions (roles in diseases).

Aminoacyl-tRNA synthetases (aaRSs)[2] play essential roles in mediating genetic information transfer from mRNAs to proteins and attach amino acids to their cognate tRNA molecules in a two-step reaction. In the first step of the reaction, the enzymes catalyze the condensation between ATP and the specific amino acid to generate an aminoacyl-adenylate intermediate. In the second, they transfer the activated amino acid to the acceptor stem of cognate tRNA to form the product aminoacyl-tRNA. The 20 aaRSs can be grouped into two distinct classes based of the conservation of primary sequences and quaternary structures (1–7). Glycyl-tRNA synthetase (GlyRS) is a class II enzyme and possesses three conserved signature motifs at the active site. However, different from other aaRSs, the quaternary structures of GlyRSs are not conserved phylogenetically. Two oligomeric forms have been discovered in nature: whereas eukaryotic and archaeal GlyRSs form $\alpha 2$ homodimers and belong to subclass IIa, their eubacterial counterparts form $\alpha 2\beta 2$ heterotetramers and belong to subclass IIc (8–13). No significant sequence homology can be found between the two subtypes. In addition to the sequence and structure diversity, studies also show that GlyRSs only aminoacylate tRNA molecules within their own kingdoms, and cross-species glycylation is rare. This phenomenon may be attributed to the distinct discriminator base at position 73. In eukaryotes, it is an adenosine that precedes the 3′-CCA end, whereas in prokaryotes, a uridine is present (9, 11, 14, 15). Therefore, the tRNA recognition mode is an interesting problem, but it is poorly understood.

The human GlyRS (hGlyRS) is a class IIa synthetase and forms a homodimer using motif 1. Motifs 2 and 3, on the other hand, are responsible for recognizing the substrates glycine and ATP. Additionally, hGlyRS features an N-terminal WHEP-TRS domain, as well as several insertion domains named insertions 1–3 (9, 16), most of which are flexible in structure (17). Recent studies have shown that aaRSs have developed functions other than aminoacylation, such as angiogenesis (18), neural development (19, 20), and immune response (21), etc. In the last two decades, missense mutations of *GARS* (the gene encoding hGlyRS) were found to be associated with Charcot-Marie-Tooth disease (CMT) subtype 2D. CMT is one of the most commonly inherited neurological disorders of the peripheral nervous system (22, 23), manifested by progressive distal muscle weakness and atrophy or hand and foot deformities. CMT is usually caused by inherited or *de novo* mutations in genes related to the structures and functions of myelin sheath or axon (24). Based on the nerve conduction velocity, CMT can be roughly divided into the CMT1 subtype with demyelinating and reduced nerve conduction velocities, the CMT2 subtype with axonal and moderately reduced or normal nerve conduction velocities, and the intermediate subtypes, respectively (25, 26). Subtypes are further classified according to the inheritance patterns and gene mutations, and more than 50 genes are implicated in various subtypes (24, 27). CMT subtype 2D begins after young adulthood and causes more severe symptoms in hand than foot (28). To date, a combined 15 missense mutations

* This work was supported by National Sciences Foundation of China Grants 31100579 and 31270760 and Guangdong Innovative Research Team Program 2011Y038. The authors declare that they have no conflicts of interest with the contents of this article.

[1] To whom correspondence should be addressed: State Key Laboratory for Biocontrol, School of Life Sciences, The Sun Yat-Sen University, 135 West Xingang Rd., Guangzhou, Guangdong 510275, People's Republic of China. Tel.: 86-20-39332943; Fax: 86-20-39332847; E-mail: xiewei6@mail.sysu.edu.cn.

[2] The abbreviations used are: aaRS, aminoacyl-tRNA synthetases; GlyRS, glycyl-tRNA synthetase; hGlyRS, human GlyRS; RMSD, root mean square deviation; CMT, Charcot-Marie-Tooth; AMPPNP, adenosine 5-(β,γ-imido) triphosphate; MD, molecular dynamics.

(S581L is excluded because of its suspicious role in the CMT disease (29)) have been discovered in human and mouse *GARS* (19, 30–36), but the disease mechanism is not clear.

We have previously solved two cocrystal structures of hGlyRS bound with $tRNA^{Gly}$ in the presence of glycine and an ATP analog and identified critical elements involved in enzyme-tRNA interactions. In addition, we proposed a working model for the aminoacylation reaction of hGlyRS that greatly contributes to the understanding of its catalytic mechanism (37). However, in both structures we reported, insertions 1 and 3 are mostly unstructured. Insertion 1 (Ala^{145}–Asn^{225}) is located between motifs 1 and 2, and it was proposed to bind to the minor groove of 3′-end of tRNA (38); insertions 2 (Asp^{307}–Asn^{348}) and 3 (Val^{440}–Val^{504}) are only found in eukaryotic GlyRSs, and their functions are not fully understood (17). Because of the disorder, the roles of the insertions 1 and 3 are uncertain in catalysis, although we speculated that they are responsible for the binding to different regions of tRNA (37). Here, we report two new crystal structures with improved resolution, with or without the tRNA substrate. We resolved the entire insertion 3 in both structures, as well as partial insertion 1 in the tRNA-bound complex. Insertion 3 acts like a conformational "switch" to control the binding of tRNA, and it is absolutely critical to aminoacylation. The structural information presented here allows for a better understanding of hGlyRS catalysis and provides new insight into the enzyme mechanism of eukaryotic GlyRSs.

Experimental Procedures

Cloning, Expression, and Purification of hGlyRS and Mutants—hGlyRS (accession no. BAA06338) contains 739 residues, and its first 54 residues encode a mitochondria localization signal peptide. The cytosolic portion of hGlyRS (designated as WTFL, including residues 56–739) was amplified from the HeLa cell line cDNA library and ligated into pET-21b (+) vector (EMD Biosciences) using the restriction sites NdeI and XhoI. The WHEP-TRS domain-truncated form of WT GlyRS (WTSF, where "SF" represents "short form") was amplified and subcloned with the same restriction sites, containing 637 residues (residues 114–739 plus the cloning sites). The apo form of full-length E71G (E71GFL) was generated by the QuikChange method (Stratagene) using WTFL as the template, whereas the WHEP-TRS-truncated form of the E71G/C157R double mutant (E71G/C157RSF) and the mutants for activity assays were produced by QuikChange PCRs using WTSF as the template. Mutants with multiple mutations in WTSF were created by consecutive QuikChange PCRs. The primers used in this study are listed in Table 1.

The expression and purification of GlyRS and mutants is the same as the protocol described by Qin *et al.* (37). All the purified mutants displayed a symmetrical peak on the size exclusion column, suggesting that they were well folded.

Crystallization, Data Collection, and Structure Determination—E71GFL was crystallized in 13–15% PEG 6000, 0.1 M sodium citrate buffer (pH 5.5), and 0.1 M NaCl. For crystallization of the tRNA-bound complex, E71G/C157RSF was mixed with $tRNA^{Gly}$ in 1:1.2 molar ratio in a buffer with 4 mM glycine, 4 mM adenosine 5-(β,γ-imido) triphosphate (AMPPNP), 5 mM

TABLE 1
The QuikChange primers used in this study
The mutated bases are underlined in the sense primers.

Gene	Sense Primers	Antisense Primers
C157R	5′-GACGTAAAAAATGGAGAAGTTTTCGTGCTGACCATC-3′	5′-GATGGTCAGCACGAAAACGTTCTCCATTTTTTACGTC-3′
E71G	5′-GATGATATTGTAGACCGAGCAAAAATGGGAGATACCCTGAAGAGGAGGTTTTTTCTATG-3′	5′-CATAGAAAAACCTCCTCTTCAGGGTATCTCCCATTTTTGCTCGGTCTACAATATCATC-3′
R420C	5′-CTCCTGTCATGCATGTGCCACCAAAGTCC-3′	5′-GGACTTTGGTGGCACATGCATGACAGGAG-3′
C468A	5′-GTATCTTGCCATTGCTGATGAGTGCTAC-3′	5′-GTAGCACTCATCAGCAATGGCAAGATAC-3′
R420C/C417A	5′-GCTGTTATGACCTCTCCGCTCATGCATGTGCCACC-3′	5′-GGTGGCACATGCATGAGCGGAGAGGTCATAACAGC-3′
C471A/C468A	5′-GTATCTTGCCATTGCTGATGAGGCATAC-3′	5′-GTATGCCTCATCAGCAATGGCAAGATAC-3′
C471A	5′-GCCATTTGTGATGAGGCATACATTACAGAAATG-3′	5′-CATTTCTGTAATGTATGCCTCATCACAAATGGC-3′
V513P	5′-CAGAAAACACTATATCCGGAAGAAGTTGTTCC-3′	5′-GGAACAACTTCTTCCGGATATAGTGTTTTCTG-3′
V441P	5′-CAGTCAATGTTCCTCAGTTTGAAC-3′	5′-GTTCAAACTGAGGAACATTGACTG-3′
G451V	5′-AAGGGAGCAATTGTTAAGGCATATAAG-3′	5′-CTTATATGCCTTAACAATTGCTCCCTT-3′
Del 432–436	5′-ACAGTCAATGTTGTTC-3′	5′-TTTCTCAGCTACAAG-3′
Del 447–456	5′-GATGCAAAACTGGTGATG-3′	5′-ACTGGGTTCAAACTGAAC-3′
Del Ins3	5′-CTATATGTGGAAGAAGAAGTTGTT-3′	5′-AACAACTTCTTCTTCCACATATAG-3′
Del Ins1	5′-AGCAAATTTGTCTACATGGCCAGAGG-3′	5′-AACTTAATGTTCAAGACTTT-3′

β-mercaptoethanol, and 5 mM $MgCl_2$. The complex was incubated on ice for 30 min and filtered before crystallization. Cocrystals were found in 27% PEG 6000, 0.1 M NaCl, 0.1 M MES (pH 6.5). After optimization, the best crystals were produced by mixing the sample of the complex, reservoir solution, and the additive E9 from the Silver Bullets screen (39) containing 0.2% (w/v) 4-diaminobutane, 0.2% (w/v) cystamine dihydrochloride, 0.2% (w/v) diloxanide furoate, 0.2% (w/v) sarcosine, 0.2% (w/v) spermine, 0.02 M HEPES sodium (pH 6.8) in a 2:1:1 ratio (v/v). All crystals were grown at 25 °C, and the fully grown crystals were soaked for 1–3 min in a cryoprotective solution containing all the components of the reservoir solution plus 20% (v/v) glycerol. The soaked crystals were mounted on a nylon loop and flash frozen in liquid nitrogen.

Native data of both forms of crystals were collected at −173 °C using Beamline 17U at the Shanghai Synchrotron Radiation Facility (Shanghai, China). The data were processed with the programs HKL 2000 (40). The space group of the E71G/C157RSF-$tRNA^{Gly}$-AMPPNP cocrystals belongs to $P2_12_12$ with a diffracting resolution of 2.90 Å, whereas that of E71GFL belongs to $P4_32_12$ with 2.75 Å resolution. The structures of E71GFL and the E71G/C157RSF-$tRNA^{Gly}$-AMPPNP complex were solved by molecular replacement, using Phenix (41) with structures of the free WT GlyRS and of the E71GSF-$tRNA^{Gly}$-AMPPNP-glycine complex as the search probes, respectively (Protein Data Bank codes 2PME and 4KR2) (17, 37). The initial models generated by molecular replacement were manually built with the program coot (42). Extra densities of insertion 3 were evident in both structures, and they were built manually according to the maps. The rebuilt models were refined with the program phenix.refine (43). Multiple cycles of refinement alternates with model rebuilding. The final *R* factors (R_{work}/R_{free}) were 0.214 and 0.265 for the E71G/C157RSF-$tRNA^{Gly}$-AMPPNP complex and 0.21 and 0.255 for E71GFL (Table 2). The Ramachandran plots of the final models have 91.7, 6.55, and 1.75% residues in the most favorable, generously allowed, and disallowed regions for the E71G/C157RSF-$tRNA^{Gly}$-AMPPNP complex and 94.89, 4.44, and 0.67% residues in the most favorable, generously allowed, and disallowed regions for the apoenzyme, respectively. The data collection and refinement statistics are listed in Table 2. The atomic coordinates and structure factors have been deposited in the Protein Data Bank with the accession codes 4KQE (apoprotein) and 4QEI (the tRNA-bound complex), respectively. The structural figures were created with PyMOL, and the domain architecture was prepared with DOG (44).

Aminoacylation Assay—The assay mixture contains 150 mM HEPES (pH 7.5), 20 mM KCl, 4 mM $MgCl_2$, 2 mM DTT, 3 mM ATP, 20 μM L-glycine, 2 μM L-[^{3}H]glycine, and 5 μM annealed $tRNA^{Gly(CCC)}$. 25 nM WTSF or mutants were added to initiate the reaction. The reaction was carried out at ambient temperature, and aliquots were removed at designated time points, spotted onto TCA-soaked filter pads, washed twice with cold 5% trichloroacetic acid, and washed twice with 95% ethanol. The filter pads were dried and measured by scintillation counting.

For the oxidation-reduction experiments, no reducing agent was added during the protein purification process. The protein oxidation was carried out by incubation of the enzyme or cysteine to alanine mutants with 1 mM oxidized glutathione for 1 h, whereas the reduction was carried out by treatment of the proteins with 10 mM DTT for 12 h after dialyzing away the extra oxidized glutathione. Then activity assays were performed with the above procedure, except the enzyme concentration was increased to 50 nM.

TABLE 2
Data collection and refinement statistics

Crystals	E71G/C157RSF-$tRNA^{Gly}$-AMPPNP	E71GFL
Data collection		
Space group	$P2_12_12$	$P4_32_12$
Cell dimensions (Å)		
a, *b*, *c* (Å)	134.605, 88.446, 81.206	91.239, 91.239, 246.614
α, β, γ (°)	90, 90, 90	90, 90, 90
Resolution (Å)	50-2.90 (3.00-2.90)[a]	50-2.75 (2.85-2.75)
R_{merge}[b]	0.122 (0.495)	0.17 (0.966)
$I/\sigma_{(I)}$	13.77 (5.47)	11.7 (2.53)
Completeness (%)	99.7 (100.0)	99.30 (99.0)
Redundancy	5.8 (6.3)	7.1 (7.0)
Refinement		
Resolution (Å)	36.90-2.90 (3.01-2.90)	34.67-2.75 (2.84-2.75)
No. reflections	22,329	28,038
R_{work}[c]/R_{free}[d]	0.214/0.265	0.210/0.255
No. atoms		
Protein	4232	4650
tRNA	1476	
Ligand	23 (AMP)	6 (Glycerol)
Water molecules	33	100
B-factors (Å^2)		
Protein	60.0	56.77
tRNA	74.1	
Ligand	46.5 (AMP)	
Water molecules	49.2	49.4
RMSD		
Bond lengths (Å)	0.012	0.003
Bond angles (°)	1.75	0.785

[a] The values in parentheses are for the highest resolution shell.
[b] $R_{merge} = \Sigma |(I - <I>)|/\sigma(I)$, where *I* is the observed intensity.
[c] $R_{work} = \Sigma_{hkl}||F_o| - |F_c||/\Sigma_{hkl}|F_o|$, calculated from the working data set.
[d] R_{free} is calculated from 5.0% of data randomly chosen and not included in refinement.

RNA Transcription and Labeling—The protocol for *in vitro* transcription of the tRNA substrates follows the same procedure as described previously (37). For 5′-end radiolabeling of tRNA, 0.5 μg of $tRNA^{Gly(CCC)}$ was incubated in a 30-μl reaction mixture consisting of 1× T4 polynucleotide kinase buffer, 1 μl of [γ-^{32}P]ATP (6,000 Ci/mmol, 1.7 μM; PerkinElmer Life Sciences), and 1 μl of T4 polynucleotide kinase (10 units/μl; Thermo Scientific). The reaction was incubated at 37 °C for 30 min. The labeled product was cleaned with a Zymo-Spin IC Column (Zymo Research) and eluted with 60 μl of TE buffer (20 mM Tris-HCl (pH 8.0) and 1 mM EDTA) containing 20 mM Tris-HCl (pH 8.0) and 1 mM EDTA.

Electrophoretic Mobility Shift Assay—To calculate approximate K_d values between hGlyRS and tRNA, 1 μl of 5′-labeled $tRNA^{Gly(CCC)}$ (>5 × 10^3 cpm) was incubated with various concentrations of purified WT GlyRS or mutants (0.5–16 μM). The protein-tRNA complexes were formed in 15 μl of a binding buffer containing 40 mM Tris-HCl (pH 8.0), 40 mM KCl, 20 mM $MgCl_2$, 2 mM glycine, 2 mM AMPPNP, and 2 mM DTT for 30 min at 25 °C before being loaded into 6% native polyacrylamide gels (pH 8.5). The gel was run at 4 °C at 14.0 V/cm after a prerun for 1 h, with a running buffer of 40 mM Tris acetate (pH 8.5). The samples of complexes were mixed in equal volumes with a sample buffer of 6% glycerol and 0.1% bromphenol blue. After electrophoresis, the gel was removed from the apparatus,

wrapped in Saran Wrap, and exposed to a phosphorimaging plate overnight. The plate was scanned with a Typhoon scanner (GE Healthcare), and the resulting band intensities were quantified using the software ImageJ. The approximate K_d values were derived from the equation $tRNA_{bound}/tRNA_{total} = [protein]/(K_d + [protein])$.

Inorganic Pyrophosphate Exchange Assay—A typical reaction mixture contained 50 mM HEPES (pH 7.5), 10 mM $MgCl_2$, 150 mM KCl, 2 mM DTT, 1 mM ATP, 4 μM [^{32}P]pyrophosphate (91 mCi/ml; PerkinElmer Life Sciences), and 1 mM glycine. The reactions were initiated by the addition of the enzyme or mutants at 100 nM, and aliquots were taken at different time points and spotted on a cellulose polyethyleneimine TLC plate (Merck Millipore). The spots were 2 cm from the bottom of the plate and 1 cm apart, and the plates were developed in 750 mM KH_2PO_4 and 4 M urea for 40 min at 25 °C in a glass jar. Then the TLC plates were exposed to a phosphorimaging plate for 50 min. The plate was scanned with a Typhoon scanner (GE Healthcare), and the intensity of the resulting bands was quantified using the software ImageJ. The fractions of ATP were calculated from the ATP/(ATP + PPi) ratios. All time points were performed in duplicate.

Molecular Dynamics (MD) Simulations—Simulations were performed with a parallel implementation of the GROMACS package (45), version 4.5.5, using the Charmm force field (46). The complex was solvated in a rhombic dodecahedron box of 52,566 TIP3P water molecules (47) with periodic boundary condition. The minimum distance between the solute and the box boundary was set to be 12 Å. The energy of the system (protein and waters) was minimized by the steepest descent method, until the maximum force was smaller than 2000 kJ*mol^{-1} nm^{-1}. 159 Na^+ and 151 Cl^- ions were added to neutralize the system and created an ionic concentration of 0.15 M. The system was subjected to energy minimization again employing the steepest descent and conjugate gradient algorithm, respectively, until the maximum force on any atom was smaller than 220 kJ*mol^{-1} nm^{-1}. A 100-ps equilibration simulation run with positional restraint was firstly performed, using a force constant of 1000 kJ*mol^{-1} nm^{-2}. Initial atomic velocities were generated according to a Maxwell distribution at 310 K. The production MD was run for 20 ns using the Verlet integration scheme (48) with a time step of 2 fs and the NPT condition (49). The pressure was kept to 1 bar with a relaxation time of 0.5 ps, and the compressibility was 4.5*10^{-5} bar^{-1}. Protein, solvent, and ions were coupled separately to a temperature bath of 310 K by using a velocity rescaling thermostat (50), with a relaxation time of 0.1 ps. Covalent bonds were constrained using the LINCS algorithm (51), whereas the cutoff distances for the Coulomb and van der Waals interactions were set to be 0.9 and 1.4 nm, respectively. The long range electrostatic interactions were treated by the Particle Mesh Ewald (PME) algorithm (52), with a tolerance of 10^{-5} and an interpolation order of 4. Structure visualization was performed with VMD (53).

Results

Two Distinct States of hGlyRS with or without the tRNA Substrate—We have previously solved the cocrystal structure of the E71GSF-tRNA^{Gly}-AMPPNP-glycine complex. E71G is a CMT-causing mutation located adjacently to the WHEP-TRS domain, with slightly elevated aminoacylation activity over WT. From our modeling studies, it possibly forms a more stable complex than WT, and this prediction was confirmed by better electron density map and moderately improved diffraction resolution of E71G cocrystal structure over WT (37). The two structures that we present in this work are still based on this variant: the full-length version of E71G (E71GFL) and the E71G/C157R double mutant. C157R is another CMT variant, and mutation of this insertion 1 residue causes grip strength deficit in mice (54). Our modeling studies have shown that C157 is close to tRNA 5′ terminus, and consequently the mutant presumably attracts the negatively charged tRNA. We therefore created the E71G/C157R double mutant for crystallization of the tRNA-bound complex. By incorporating a second mutation with a similar effect, we would expect a more stable enzyme-tRNA complex. The structural findings from the two structures are described below.

The space group of the full-length apoenzyme E71GFL belongs to $P4_32_12$, and each asymmetric unit contains a monomer (Protein Data Bank code 4KQE). The biological homodimer is generated from the monomer in the asymmetric unit by a crystallographic 2-fold axis. The crystals were grown in a similar condition to the full-length WT protein, with a slightly higher concentration of PEG 6000 and a lower pH (pH 5.5 *versus* 6.5). The polypeptide in the final model is visible from Ile^{64} to Gly^{674}, except for the two short internal disordered regions of Met^{383}–Ala^{387} and Thr^{510}–Tyr^{512}. The N terminus including the WHEP-TRS domain (Leu^{13}–Asp^{63}), and the 17 residues at the C terminus, including the His_6 tag, are disordered (Fig. 1*A*).

The catalytic domain (Ile^{64}–Val^{556}) is formed by eight mixed β-strands surrounded by α-helices on both sides. The C-terminal anticodon binding domain (Val^{556}–Lys^{680}) displays the typical α/β fold shared by class IIa synthetases (Fig. 1*B*). The protein structure closely resembles WT (Protein Data Bank code 2PME), and their RMSD is 0.7 Å (over 519 Cαs). The most apparent difference is the ordering of insertion 3 in the current structure (Fig. 1*C*). A β-hairpin structure in newly resolved insertion 3 (β17 and β18) packs against three small α-helices (α14–α16), and the ends of insertion 3 are capped by another pair of antiparallel β-strands (β17 and β20) (Fig. 1*D*). Judging from the structure, it is more reasonable to redefine insertion 3 as the Ala^{428}–Val^{516} fragment. The newer version is slightly longer than the previous one (Val^{440}–Val^{504}) (9) and includes the β17-β20 hairpin structure. Additionally, insertion 3 appears to be "hollow" on the inside, suggesting a more loosely packed structure with high flexibility (Fig. 1*B*). We also, for the first time, observed the CMT-related residue Asp^{500} (34), which is located on the loop β19-β20 and is exposed to the solvent.

To further explore the mechanism of protein dynamics, we crystallized the complex of the double mutant E71G/C157RSF bound with tRNA^{Gly} in the presence of glycine and an ATP analog inhibitor AMPPNP. The E71G/C157RSF complex crystals grew in a similar condition to that of the E71GSF complex (37) but did produce a structure with a better resolution (2.9 Å; Protein Data Bank code 4QEI). For crystallization purposes,

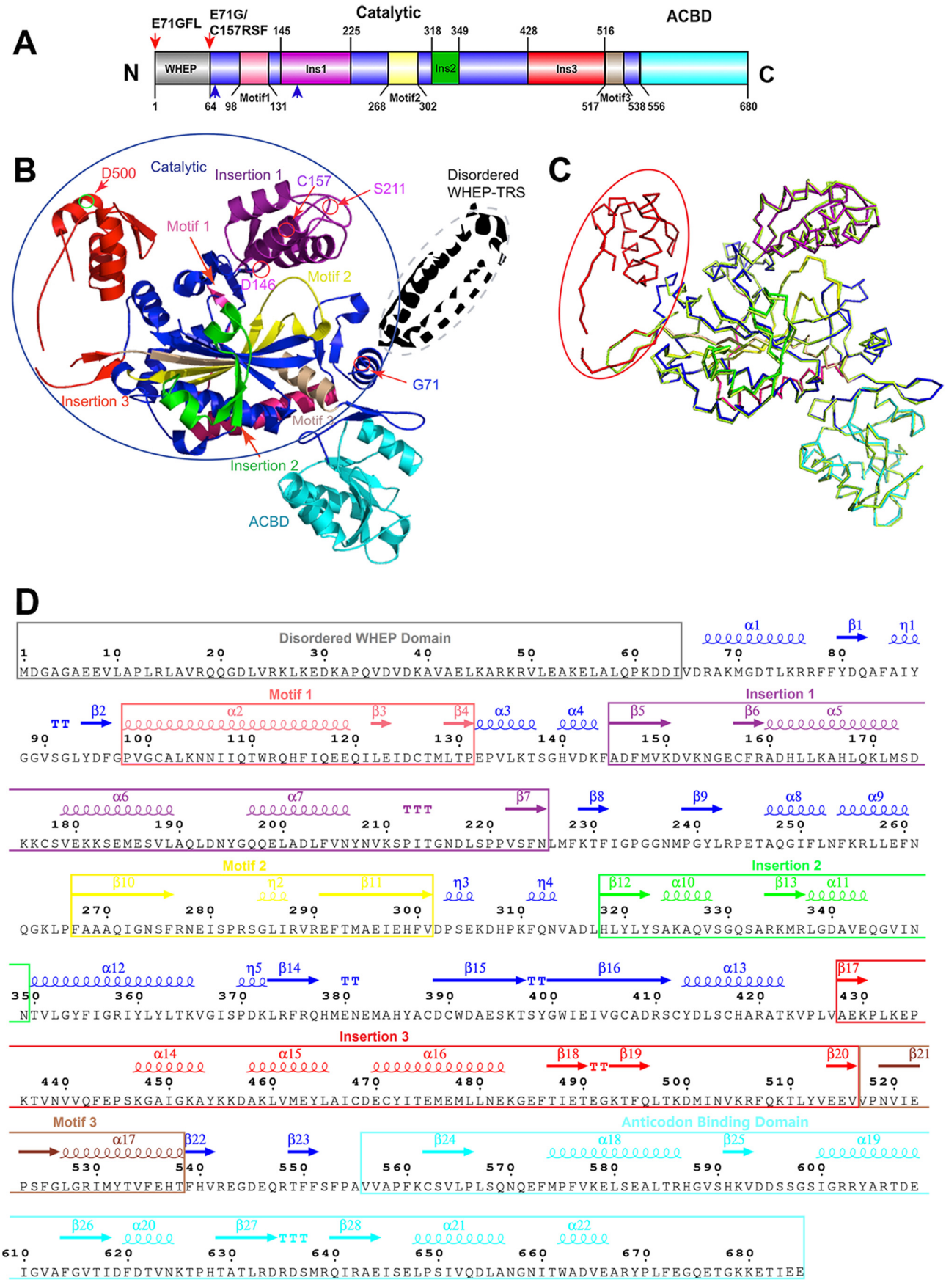

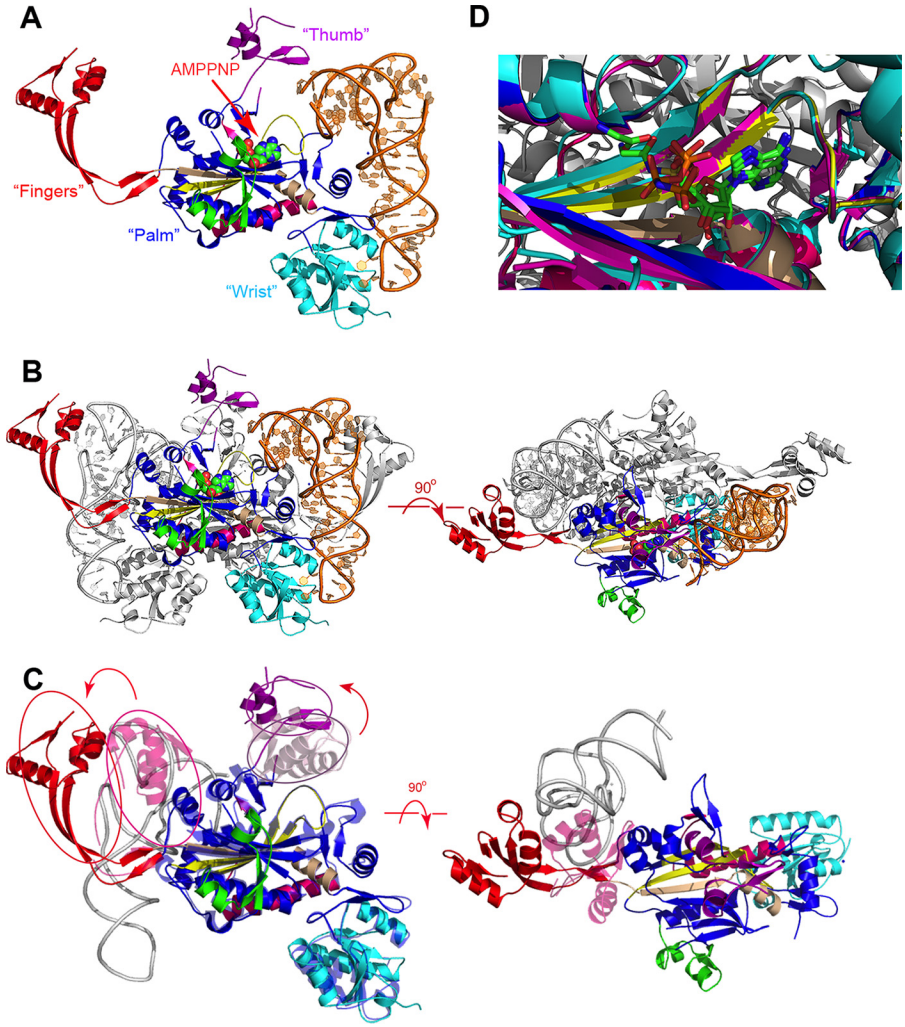

FIGURE 2. **Overall structures of the quaternary complex and conformational changes in insertion 3 on tRNA binding.** *A*, the E71G/C157RSF-tRNA^{Gly}-AMPPNP complex in an open conformation. tRNA is in *orange*, whereas glycine and AMPPNP are in space-filling representation. The shape of the protein is labeled as parts of a hand. *B*, two orthogonal views of the dimer complex in ribbon rendition. The occupied monomer is colored as in Fig. 1*A*, whereas the other subunit is colored *gray*. *C*, the overlay of the structure of apo E71GFL and E71G/C157RSF-tRNA^{Gly}-AMPPNP complex. Although the AD domains superimpose well, both insertions show large displacements upon tRNA binding as indicated by the *red arrows*. The two insertions are *circled*. *D*, the structure superposition of E71G/C157RSF-tRNA^{Gly}-AMPPNP complex (Protein Data Bank code 4QEI), GlyRS-GlySA complex (Protein Data Bank code 2ZT8, *purple*), and E71GSF-tRNA^{Gly}-AMPPNP-glycine complex (Protein Data Bank code 4KR3, *cyan*). The AMPPNP moiety in all three structures superpose well.

the flexible WHEP-TRS domain was not included during cloning. In the refined model, we resolved Ile^{64}–Leu^{171}, Gln^{198}–Asn^{206}, Phe^{224}–Glu^{380}, Asp^{389}–Thr^{490}, and Gln^{496}–Lys^{680} fragments of the protein and the entire tRNA substrate except for the last four nucleotides at the 3′ terminus. Additionally, the final model contains one AMP (coming from AMPPNP) and 33 water molecules (Table 2). Insertion 3 is visible and the catalytic region in the complex is highly similar to that of apoprotein or E71GFL (Fig. 2*A*). However, insertions 1 and 3 undergo large conformational changes and extend to the solvent. The protein in the complex adopts a fully "open" conformation, making a shape of a hand. Insertion 3 (the "fingers" domain) is almost completely structured and retains a similar fold as observed in E71GFL. The original broken loops in insertion 3 of E71GFL (Pro^{435}–Val^{441} and Thr^{510}–Tyr^{512}) reorder and extend the original β17-β18 hairpin to form two long, remarkable antiparallel β-strands. Insertion 1 (the "thumb" domain) becomes partially disordered (two helices are resolved in this region) because of the hindrance with tRNA 3′-end. In our previously reported cocrystal structures with tRNA^{Gly}, both insertions are disordered (37). Modeling studies indicate that insertion 3 from the other subunit would block the

FIGURE 1. **Overall structures of E71GFL and insertion 3.** *A*, the GlyRS domain architecture without the N-terminal mitochondria localization signal. The catalytic domain (colored *blue*) contains three insertions (Ins1–3, colored *magenta*, *green*, and *red*, respectively) and three signature motifs (motifs 1–3, colored *hot pink*, *yellow*, and *wheat*, respectively). The anticodon binding domain (ACBD) is shown in *cyan*, and WHEP-TRS domain is shown in *gray*. The *blue arrows* indicate the positions of the two mutations in sequence, whereas the *red arrows* designate the start site of the two GlyRS constructs used in this work. *B*, ribbon representation of the closed conformation of the E71GFL apoenzyme. The color scheme is as in Fig. 1*A*. The disordered WHEP-TRS domain is modeled in and *circled* by the *broken gray oval*. The positions of CMT-causing residues Gly^{71} and other four residues falling into insertions 1 and 3 (Asp^{146}, Ser^{211}, Asp^{500}, and Cys^{157}) are indicated and labeled in the structure. *C*, structure comparison of the WT enzyme (*yellow*) and E71GFL (color scheme as in *A*). The resolved insertion 3 in E71GFL is noted by the *red oval*. *D*, the color-coded secondary structure of E71GFL. The α-helices, β-sheets, and β-hairpins are denoted as α, β, and η, respectively.

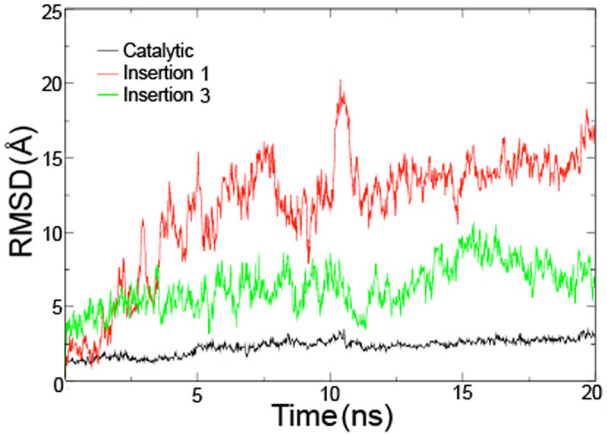

FIGURE 3. **MD simulation of insertions 1 and 3 on a 20-ns scale.** The *vertical axis* represents the RMSD of the insertions off their normal positions. The insertion 1 is colored in *red*, and the insertion 3 is colored in *green*. Insertion 1 undergoes larger conformational changes (RMSD 11.8 Å on average) than insertion 3 (RMSD 6.3 Å). The catalytic domain (*black curve*) serves as an internal control.

entrance of the incoming tRNA molecule. In the current structure, insertion 3 is detached from the catalytic domain (the "palm" domain) and reaches out to the solvent. After we regenerated the biological dimer using the 2-fold axis, we found that tRNA fits well in the "grasp" of insertion 3, and the protein and RNA form a complex in 2:2 stoichiometry (Fig. 2*B*). Structure comparison of the protein in the presence and absence of tRNA indicates that the two domains experience large conformational changes (Fig. 2*C*). In contrast, the rest part of the complex including the tRNA molecule nearly resembles the E71GSF-tRNA-AMPPNP-glycine structure published elsewhere (37) and will not be further discussed. However, in the active site, only the density of AMP is found. The interactions with AMP are conserved and the position are almost identical to the AMP moiety in the E71GSF-tRNA-AMPPNP-glycine complex structure (Fig. 2*D*) (37, 55). The density of glycine on the other hand is not evident and not modeled.

The Flexibility of Insertions 1 and 3 by MD Simulations—Insertions 1 and 3 are two highly mobile domains as suggested by our crystal structures, and we next performed MD Simulations on the free E71GFL structure to analyze the flexibility of both domains. After analyzing the 20-ns simulation trajectory, we obtained some conformations that were between the two crystal structures (the apo- and tRNA-bound forms). Among these conformations, we found that two regions, residues Ala^{428}–Val^{516} and residues Ala^{145}–Asn^{225}, display larger flexibility than others in the apoprotein, which match well the definitions of two insertions in our structure. Ala^{428}–Val^{516} (insertion 3) constantly "wander" from its equilibrium position, with an average RMSD 6.3 Å and the largest one 10.8 Å. Ala^{145}–Asn^{225} (insertion 1) shows an average RMSD of 11.8 Å with the largest one 20.2 Å (Fig. 3). Additionally, insertion 3 might go through a fast equilibrium perturbation in solution, creating possibilities for the binding of the tRNA substrate. The flexibility of these two regions is related to the transition from its apo state to the substrate-bound state, which is also exhibited by our crystal structures.

Conformational Changes of Insertion 3 Are Critical for Aminoacylation—Two regions of insertion 3 make principal contacts with tRNA: Leu^{511}–Val^{513} and Leu^{432}–Lys^{436} (the hinged loops), which connect the β17-β20 hairpin structure that runs across the variable region of tRNA (G43 and C44); and the Lys^{447}–Lys^{456} helix, which packs against the G19–C56 base pair of tRNA elbow (Fig. 4*A*). Specifically, Glu^{429} side chain makes a hydrogen bond with the O_2' atom of C44, and the phenyl ring of Tyr^{512} stacks onto the backbone phosphate of G43 (Fig. 4*B*). To study the importance of the structural reorganization to enzyme functions, we introduced a series of mutations and assessed the contribution of individual residues or motifs in insertion 3 to aminoacylation through activity assays. To measure activities, we chose two time points (2 and 5 min) in which the initial velocities of WT fall into the linear range. We first deleted the entire insertion 3, and the deletion remarkably reduced its activity to less than 1% of WT activity. This result suggests that insertion 3 greatly influences tRNA binding ability of the enzyme. As the reference, the activity of the C157R single mutant is 62% of WT (Fig. 4*C*), whereas the E71G/C157R double mutant is only 20%. We are currently not clear about the cause of the particularly low activity of the double mutant. We next tested the deletion of the Leu^{432}–Lys^{436} fragment, which totally abolished enzymatic activity. We also created the V441P mutant to prevent the full opening of insertion 3 by introducing a proline residue (backbone restrictions to break the β-strand pattern), and this mutation reduced the activity by 47%. Moreover, the Lys^{447}–Lys^{456} helical region is rich in basic residues and forms a positive patch to interact with the elbow region of tRNA: the NZ atom of Lys^{447} may form a salt bridge with U20 phosphate oxygen; the carbonyl oxygens of Gly^{451} and Lys^{455} form a total of three hydrogen bonds with the base and the sugar ring of C56 (Fig. 4*D*). The deletion of the Lys^{447}–Lys^{456} helix greatly impaired aminoacylation, and only 61% activity was left. Because the interactions at this region are mainly nonspecific and two glycine residues, Gly^{448} and Gly^{451}, are probably the prerequisite for the structural complementarity, we mutated Gly^{451} to a valine to increase the hindrance with tRNA, and the mutant only retained 40% of the activity of WT. A prominent feature of insertion 3 is the formation of two extended antiparallel β-strands and forms the core structure of this domain. We introduced a proline substitution of Val^{513} on the hinged loop, which leaves the enzyme only with 22% activity.

Consequently, the conformational changes induced by tRNA binding are absolutely important to enzyme functions, and judging from the cocrystal structure, the loss of activity most likely results from the loss of tRNA binding affinity. To evaluate the substrate binding ability of each mutant, we carried out the EMSA assay. As shown in Fig. 4*E*, WTFL was able to form an enzyme-tRNA complex, as indicated by the slower moving band at the concentration of 1 μM hGlyRS, and the complex became the predominant species at 4 μM. The K_d value is determined to be 7.79 ± 1.83 μM for the WTFL enzyme. By contrast, the binding affinities of G451V and Del 447–456 were strongly impaired (84 and 48 μM, respectively), whereas the complex formation for Del Ins3 and Del 432–436 were virtually undetectable. The K_d values for other mutants range from 11 to 64

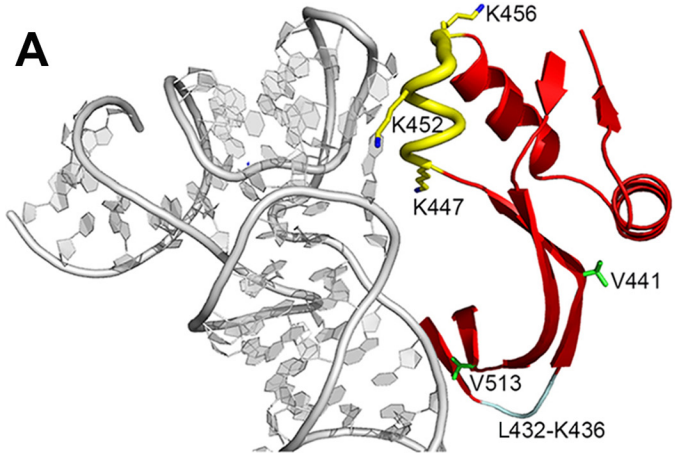

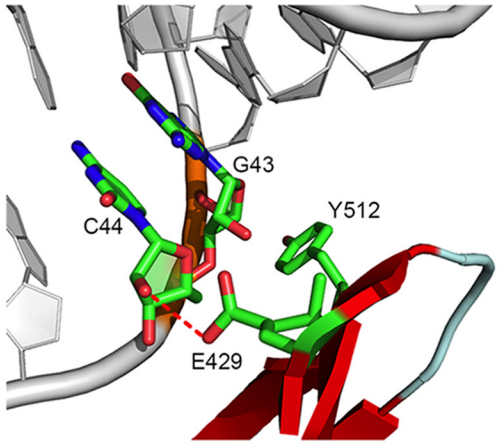

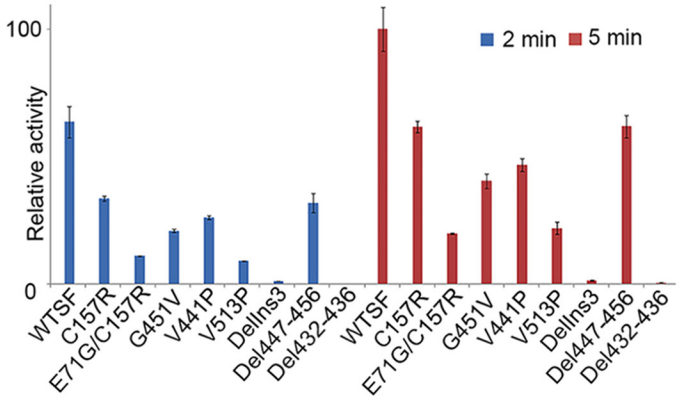

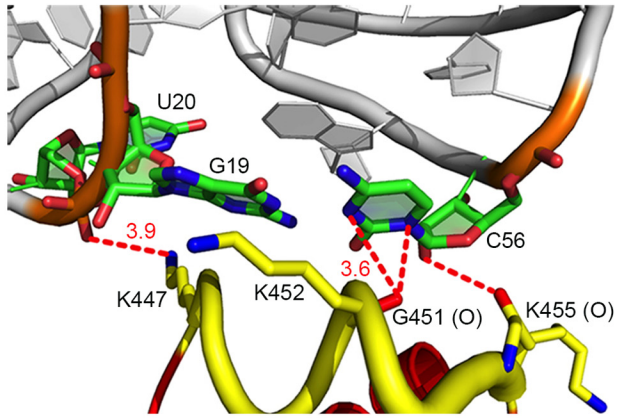

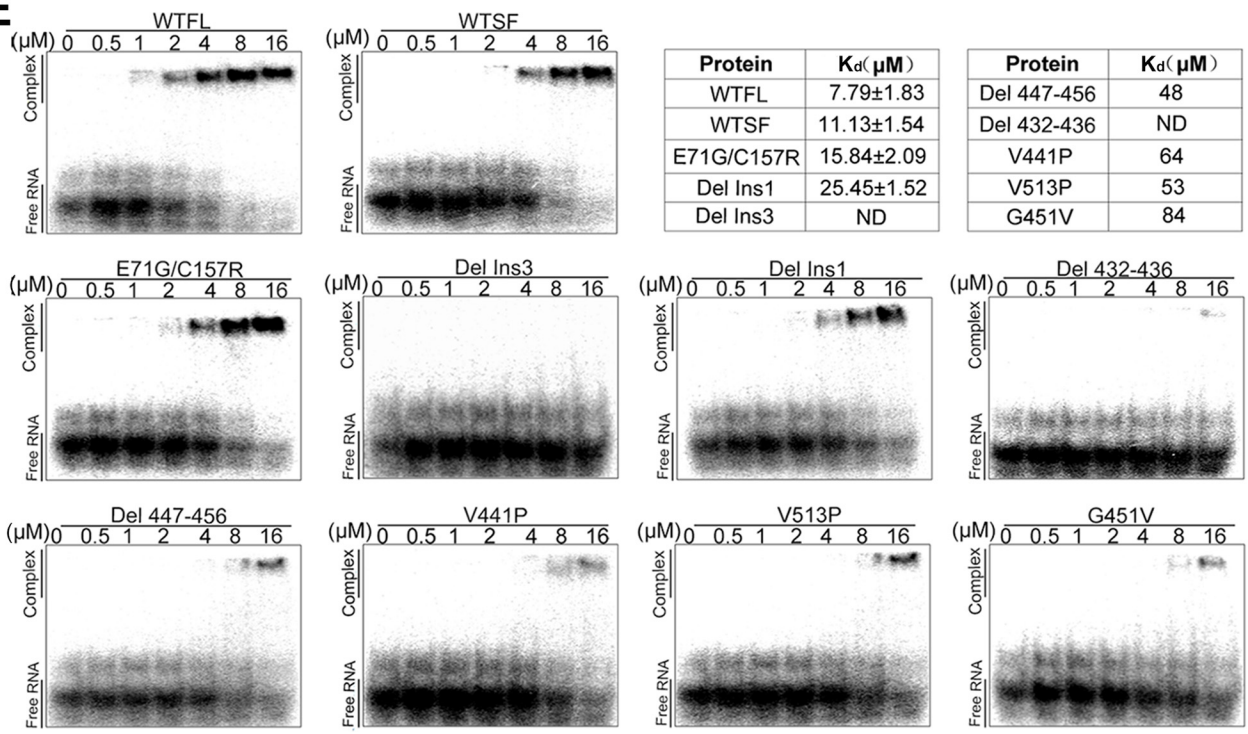

Protein	K_d(μM)
WTFL	7.79±1.83
WTSF	11.13±1.54
E71G/C157R	15.84±2.09
Del Ins1	25.45±1.52
Del Ins3	ND

Protein	K_d(μM)
Del 447-456	48
Del 432-436	ND
V441P	64
V513P	53
G451V	84

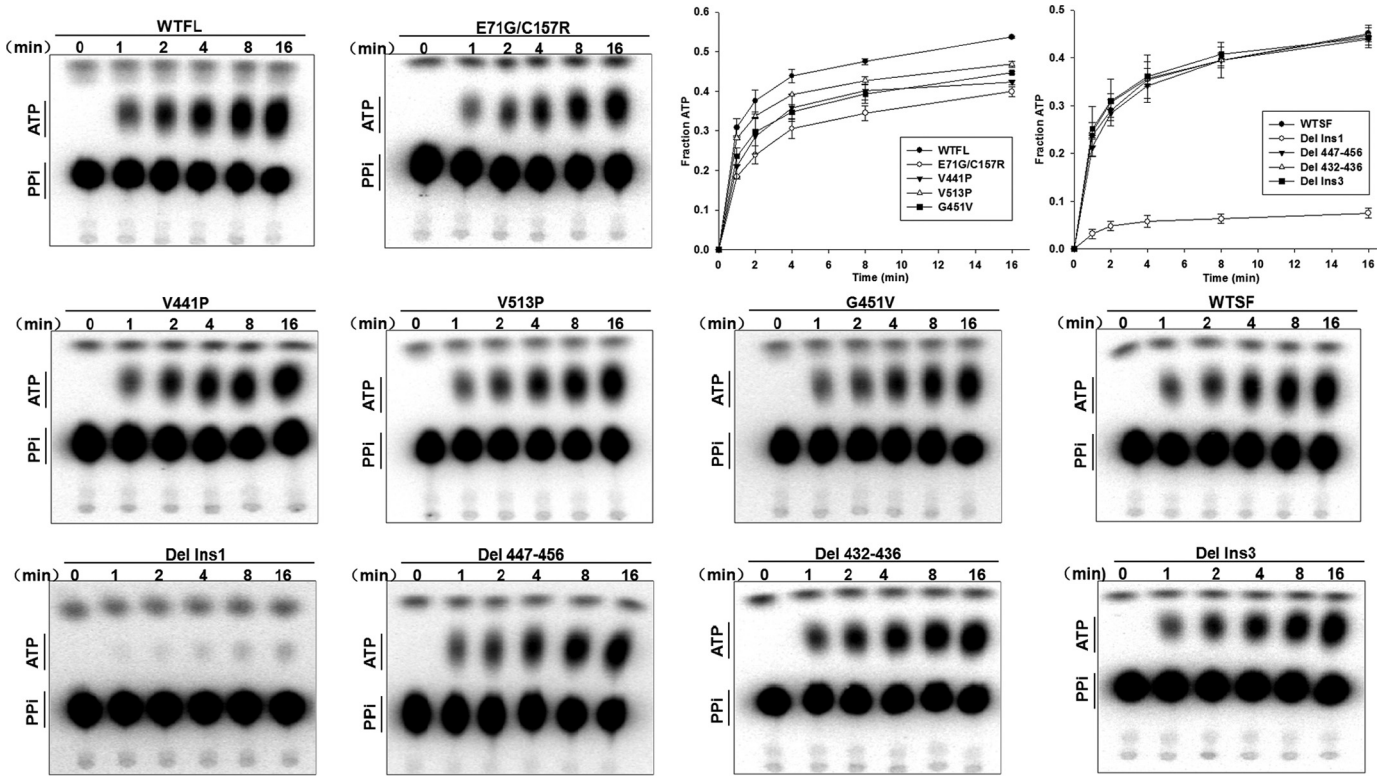

FIGURE 5. **PPi-exchange activity of WT and mutants of hGlyRS.** The reactions were carried out using 100 nM enzymes. Formation of enzyme-bound aminoacyl-adenylate intermediate allows conversion of PPi into ATP. The reactions were quenched at different time points (0, 1, 2, 4, 8, and 16 min), separated on cellulose polyethyleneimine TLC plate, and visualized by a phosphorimaging plate. As shown in the *top right corner*, the insertion 3 point mutations or deletions did not greatly affect PPi exchange activities, when compared with the WT.

μM (Fig. 4*E*), mostly in good agreement with our aminoacylation results.

To rule out the possibility that the mutations might affect the formation of the adenylate intermediate, we performed the PPi-exchange assay. As shown in Fig. 5, the PPi-exchange assays indicated that most point mutations or deletions did not affect the formation of the adenylate intermediate significantly, and their PPi exchange activities were on a similar level to that of WTSF. As a negative control, the deletion of insertion 1 greatly reduced the exchange rate, which was consistent with the notion that insertion 1 plays a critical role in the binding of glycine.

In our cocrystal structure, insertion 3 acts like a switch and makes large movements to accommodate the crossly bound tRNA molecule. We wonder what will happen if we restrain the movements of insertion 3. In the E71GFL structure, insertion 3 folds back to the catalytic domain and interacts with α13. The domain also contains two long loops (Lys^{430}–Ser^{446} and Leu^{497}–Glu^{514}), but each loop is missing a short polypeptide (Pro^{435}–Val^{441} and Thr^{510}–Tyr^{512}) (Fig. 6*A*). Additionally, Cys^{468} from insertion 3 is close to Arg^{420} on α13, and they may interact to "tie" the two domains together (Fig. 6*B*). To explore this possibility, we introduced cysteine mutations on relevant residues and tested their activities. The R420C mutant displays less than 1.2% activity of WT upon oxidation, whereas the following reduction restores its activity to 79.7% of WT, suggesting the participation of R420C in the disulfide bond on oxidation (Fig. 6*C*). As a reference, the activity of WT is not severely affected, with only a 1.43-fold difference before and after the reduction treatment (the activity "gain" suggests that oxidation is already underway during the enzyme purification process). To rule out the possibility of other disulfide bridge formations with Cys^{417} or Cys^{471}, we further mutated these two residues to an alanine, and the same trend still holds for the mutants R420C/C417A, R420C/C471A, and R420C/C417A/C471A. However, once Cys^{468} was changed to an alanine, the single mutant C468A or the quadruple mutant R420C/C417A/C471A/C468A behaves like WT, supporting our theory of the inability to form the disulfide bridge between C468A and R420C. We also tested the double mutant C417A/C471A as

FIGURE 4. **The enzyme-tRNA interactions in the quaternary complex and the activity assays.** *A*, interactions of insertion 3 and crossly bound $tRNA^{Gly}$, where tRNA is colored *gray*, and insertion 3 is colored *red*. The important residues that form contacts are shown in stick representation, and the elbow-contacting helix Lys^{447}–Lys^{456} is colored *yellow*. The detailed enzyme-tRNA interactions in the quaternary complex. *B*, the contacts between the tRNA variable region and residues from the hinged loops in insertion 3. *C*, glycylation assays for mutants of residues involved in critical tRNA recognition. E71G/C157R represents the E71G/C157RSF double mutant, and all other mutants are in the short form (no WHEP-TRS domain). Two sets of data are shown, representing the measurements at 2- (*blue*) and 5-min time points (*red*) respectively. The activity of WT hGlyRS at the 5-min time point is regarded as 100%, and the readings at time 0 of the variants are used as blanks. The activity of each mutant is compared with WT in terms of percentages, and the *error bars* were calculated from two measurements. *D*, the shape complementation between the elbow region of tRNA and the α14 helix in insertion 3. Possible interactions are indicated by the *red lines*, and distances over 3.6 Å are indicated by the *numbers*. *E*, EMSA between GlyRS mutants and $tRNA^{Gly}$. *ND*, not determined. The K_d values are derived from the equation $tRNA_{bound}/tRNA_{total} = [protein]/(K_d + [protein])$ and given in the *upper right table*.

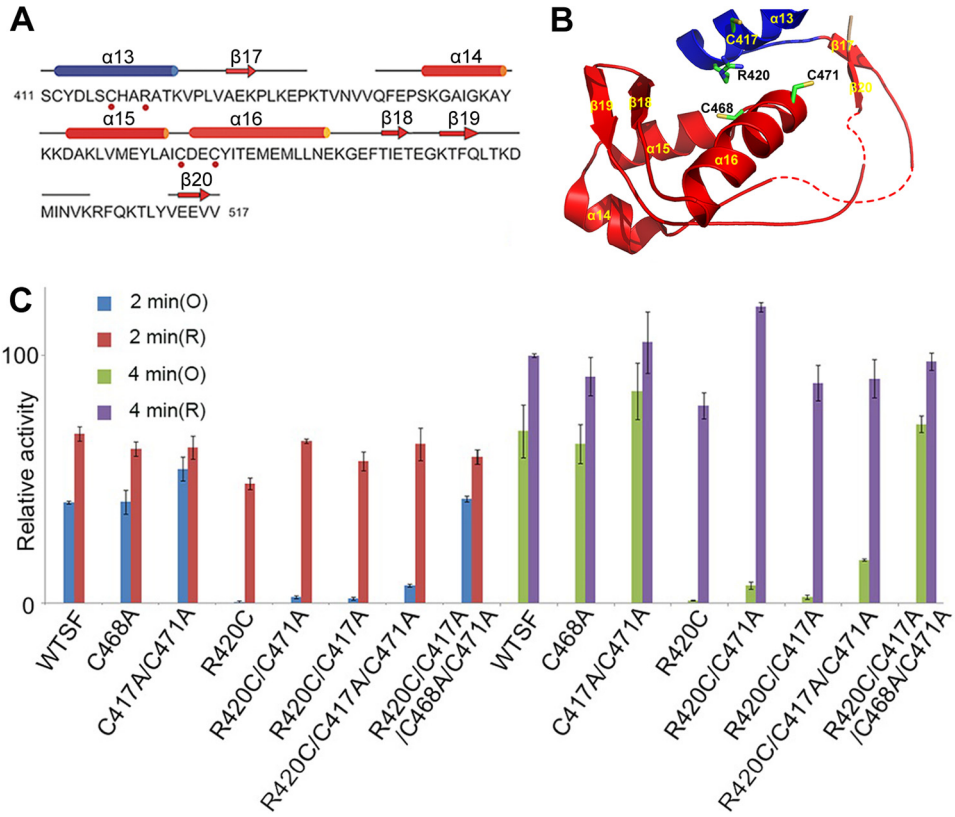

FIGURE 6. **Impacts of insertion 3 restraints on enzyme activities.** *A*, secondary structure of insertion 3 in E71GFL. The major structural elements are labeled above the sequence, whereas residues of interests are designated by *red dots* below. *B*, the close-up view of insertion 3 in E71GFL and the structural elements are labeled. Several cysteine residues are shown, and their importance is tested as described below. Cys^{468} is located on a loop between α15 and α16, whereas Arg^{420} is on α13. *C*, activity tests of the cysteine mutants. *O* indicates oxidation with 1 mM oxidized glutathione 1 h at 4 °C; *R* indicates oxidation with 1 mM oxidized glutathione for 1 h at 4 °C followed by 10 mM DTT reduction for overnight at 4 °C. Two time points were used, and the data were processed as in *C*.

another control experiment and excluded their involvement in the disulfide bond as well. These data collectively pinpoint the disulfide formation between Cys^{468} and R420C, which underscores the significance of conformational opening of insertion 3 during the binding of tRNA substrate. On the other hand, restraints on the structural rearrangements greatly diminish glycylation activity.

Discussion

Roles of Insertions 1 and 3 in hGlyRS Catalysis—hGlyRS is a multidomain enzyme, and conformational changes during aminoacylation appear to be an inherent part of its catalytic cycle. In all the previously solved structures of GlyRS and mutants in various crystal forms (with or without substrates), insertion 3 is invisible, indicating the high flexibility of this eukaryote-specific domain. Additionally, we have solved the structures of the tRNA-bound complexes. In both structures, insertion 3 is barely resolved either, visible only up to Val^{441} or beyond Phe^{507}. Based on the partial β-hairpin structure of insertion 3 and the position of tRNA, we proposed that the role of this insertion domain is responsible for tRNA binding (37). In this work, we successfully captured the electron density of this domain because of crystal lattice packing using two CMT mutations. Structure analysis reveals that crystal packing is probably responsible for the ordering of insertion 3, where residues Lys^{455}-Lys^{456} interact with Asp$^{545'}$-Glu$^{546'}$ in the tRNA-bound complex (Fig. 7*A*) (prime symbols indicate that the residues are from symmetry-related molecules). Likewise, in the apoenzyme structure, the insertion 3 domains from two different GlyRS molecules are likely tethered together by the Ser^{304}-Thr$^{437'}$ hydrogen bond, and the Glu^{514}–Lys$^{436'}$ salt bridge (Fig. 7*B*). Each of these two structures is a snapshot of the chemical reaction and represents an important state along the catalytic pathway. More importantly, by structure comparison, we discovered large conformational changes induced by tRNA binding. Additionally, structure overlay shows that the displacement of insertion 3 allows tRNA to fit in the "grip" of the hand-shaped enzyme. According to the structure features of this domain, we now redefine the domain as Ala^{428}–Val^{516}. In the apoenzyme structure, insertion 3 becomes ordered by folding back onto the catalytic domain and interacts with α13. In the closed conformation, the fingers touch and make contact with the palm. During glycylation, this domain opens up and provides the cross-subunit support for the tRNA molecule through backbone interactions. In the open conformation, part of the fingers domain acts like a "belt," and the long strands restrain the orientation of tRNA (Fig. 4*B*). The general fold of insertion 3 present in the two structures is largely preserved, suggesting that the structure is authentic. However, the crystal structures provide only static snapshots of a dynamic process, we therefore carried out MD simulations, as well as activity assays on the enzyme to explore possible dynamics. The MD results also indicate large thermal motions of the two domains of the apoen-

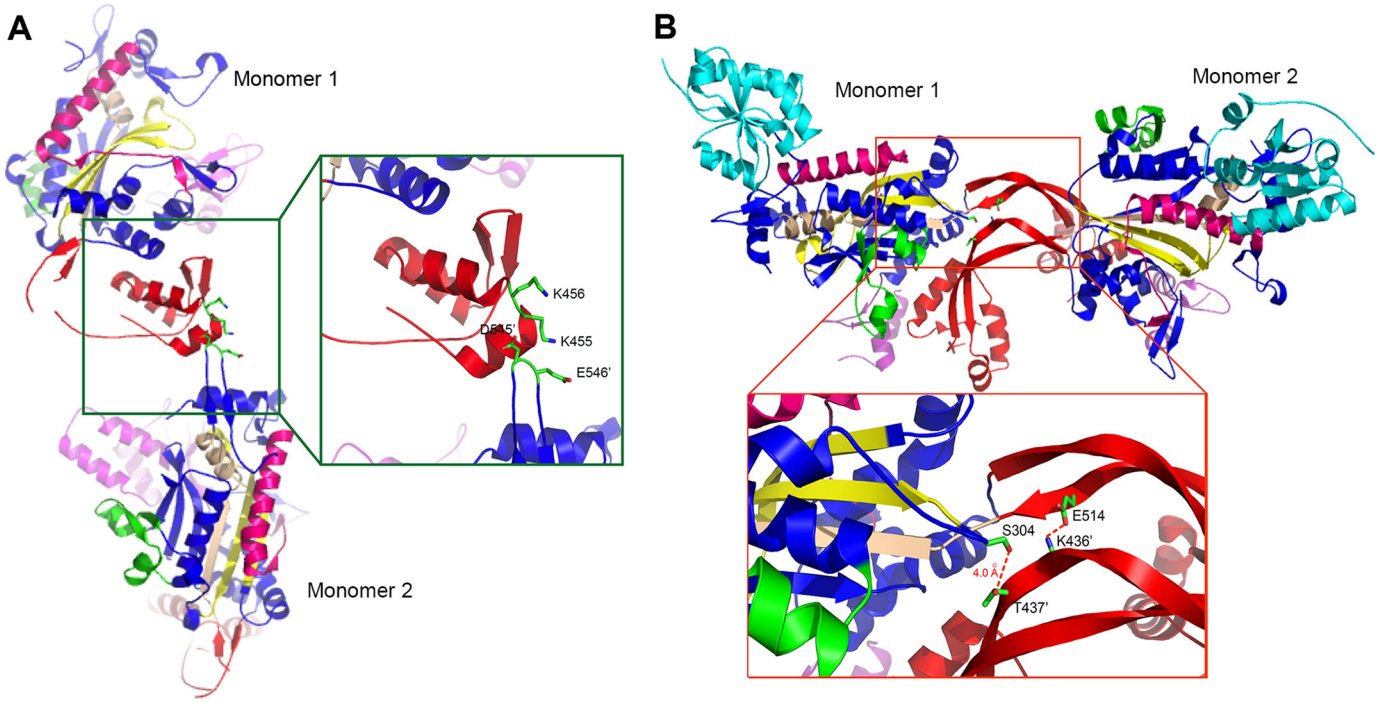

FIGURE 7. **Two crystal-packing patterns.** *A*, the crystal-packing pattern in E71GFL crystal structure, which is mainly maintained by charged interactions. *B*, the crystal-packing pattern in E71G/C157RSF-tRNA^{Gly}-AMPPNP structure. Only the protein molecules are drawn for clarity. The *red lines* indicate possible interactions.

zyme, which are consistent with the crystal structures. Taken together, the data suggest that large conformational changes of insertion 3 are an intrinsic part of the aminoacylation reaction and not of crystallization artifacts.

The large conformational changes experienced by both the enzyme and tRNA are entropically unfavorable. However, the entropic costs of the structure reorganization are compensated by the enthalpy gains accompanying with the stripping of the surface water molecules and also favorable energetic interactions in the tRNA-bound state. In this process, two hinged loops that connect insertion 3 to the catalytic domain play key roles. To test their importance, we systematically introduced point mutations or deletions in various segments that would reduce the flexibility and conducted rigorous activity analyses. These assays proved that the flexibility of insertion 3 is absolutely critical to enzyme activities.

Insertion 1 is another unstructured region in the structures of hGlyRS-tRNA complexes and is only visible in the apoenzyme (17, 37). Hence the binding of tRNA induces the changes of insertion 1 from a tightly packed domain to a loosely packed structure for tRNA minor groove interactions. The MD studies indicate an even larger flexibility for this domain. Activity assays showed that this domain is indispensable, which may be attributed to its role in binding of small substrates (37). This is probably the reason why it is a conserved domain in all GlyRSs. In contrast, insertion 3 is a eukaryote-specific addition, and it is important to tRNA binding. We searched both domains in the Protein Data Bank for their homologs but did not obtain any hits with significant structural resemblance. Therefore, the origin of neither domain is clear from a structural point view. A hypothesis on the functions of the two domains is that hGlyRS may employ these two domains to regulate the binding of small substrates and tRNA, respectively, and each insertion serves as an important switch for substrate binding. If this hypothesis were true, how GlyRSs in lower organisms efficiently bind to tRNA and why eukaryotic GlyRSs acquired these domains remain to be investigated.

Connections to CMT—Four CMT-causing residues fall into the insertion regions of hGlyRS: Ser^{211}, Cys^{157}, and Asp^{146} in insertion 1 and Asp^{500} in insertion 3. To our knowledge, Asp^{500} has not been resolved in the past, and this is the first time it becomes visible. Additionally, the positions of the first three in the presence of tRNA remained undetermined until now. All three residues have relatively large movements upon tRNA binding and have high B-factors (Cys^{157} is an arginine in the complex form). Interestingly, the corresponding CMT mutations D146N, C157R, and D500N all gain a positive charge. However, from the structure, none of them is likely to be directly involved in tRNA binding (C157R is ~7.5 Å from tRNA). It therefore remains to be seen whether the mutations have long range effects to the binding ability of tRNA.

Mutations in tyrosyl-, methionyl-, alanyl-, and lysyl-tRNA synthetases have been reported to be the causes of CMTDIC (Charcot-Marie-Tooth disease dominant intermediate type C), CMT2, CMT2N (Charcot-Marie-Tooth disease type 2N), and CMT RIB (Charcot-Marie-Tooth disease recessive intermediate type B), respectively (56–59), suggesting a role of protein synthesizing machinery in the neurodegeneration process. Both mutants that we study in this work display abnormal aminoacylation activities. aaRS mutations like these may lead to altered kinetics/thermodynamics, even though some mutants may retain activities comparable with that of WT. These mutations may also change the physical or chemical properties of aaRSs and impact their abilities to execute their functions, clas-

sical or noncanonical. Systematic investigation of disease-associated mutations in aaRSs is needed to ascertain their structural and functional characteristics potentially causing unusual binding (for example, protein-protein interactions) or aminoacylation behaviors. A recent case in point is that human SerRS has been demonstrated to bind to the promoter of vascular endothelial growth factor A to carry out its angiogenic functions (60). Such studies may offer a new perspective on the relevant causes of CMT.

Author Contributions—W. X. conceived and designed the research; X. D., X. Q., L. C., Q. J., Y. Z., and D. L. performed the research; Z. Z., G. R., Z. W., Q. L., and W. X. analyzed data; and Z. Z., G. R., and W. X. wrote the paper. All authors reviewed the results and approved the final version of the manuscript.

Acknowledgment—We thank Shanghai Synchrotron Radiation Facility for access to Beamline 17U.

References

1. Eriani, G., Delarue, M., Poch, O., Gangloff, J., and Moras, D. (1990) Partition of tRNA synthetases into two classes based on mutually exclusive sets of sequence motifs. *Nature* **347,** 203–206
2. Schimmel, P. (1987) Aminoacyl tRNA synthetases: general scheme of structure-function relationships in the polypeptides and recognition of transfer RNAs. *Annu. Rev. Biochem.* **56,** 125–158
3. Cusack, S. (1993) Sequence, structure and evolutionary relationships between class 2 aminoacyl-tRNA synthetases: an update. *Biochimie* **75,** 1077–1081
4. Perona, J. J., and Gruic-Sovulj, I. (2014) Synthetic and editing mechanisms of aminoacyl-tRNA synthetases. *Top. Curr. Chem.* **344,** 1–41
5. Srinivasan, G., James, C. M., and Krzycki, J. A. (2002) Pyrrolysine encoded by UAG in Archaea: charging of a UAG-decoding specialized tRNA. *Science* **296,** 1459–1462
6. Sauerwald, A., Zhu, W., Major, T. A., Roy, H., Palioura, S., Jahn, D., Whitman, W. B., Yates, J. R., 3rd, Ibba, M., and Söll, D. (2005) RNA-dependent cysteine biosynthesis in archaea. *Science* **307,** 1969–1972
7. Delarue, M., and Moras, D. (1993) The aminoacyl-tRNA synthetase family: modules at work. *BioEssays* **15,** 675–687
8. Dignam, S. S., and Dignam, J. D. (1984) Glycyl- and alanyl-tRNA synthetases from *Bombyx mori*: purification and properties. *J. Biol. Chem.* **259,** 4043–4048
9. Freist, W., Logan, D. T., and Gauss, D. H. (1996) Glycyl-tRNA synthetase. *Biol. Chem. Hoppe-Seyler* **377,** 343–356
10. Mazauric, M. H., Reinbolt, J., Lorber, B., Ebel, C., Keith, G., Giegé, R., and Kern, D. (1996) An example of non-conservation of oligomeric structure in prokaryotic aminoacyl-tRNA synthetases: biochemical and structural properties of glycyl-tRNA synthetase from *Thermus thermophilus*. *Eur. J. Biochem.* **241,** 814–826
11. Shiba, K., Schimmel, P., Motegi, H., and Noda, T. (1994) Human glycyl-tRNA synthetase: wide divergence of primary structure from bacterial counterpart and species-specific aminoacylation. *J. Biol. Chem.* **269,** 30049–30055
12. Surguchov, A. P., and Surguchova, I. G. (1975) Two enzymically active forms of glycyl-tRNA synthetase from *Bacillus brevis*: purification and properties. *Eur. J. Biochem.* **54,** 175–184
13. Kern, D., Giegé, R., and Ebel, J. P. (1981) Glycyl-tRNA synthetase from baker's yeast: interconversion between active and inactive forms of the enzyme. *Biochemistry* **20,** 122–131
14. Schimmel, P. (1995) An operational RNA code for amino acids and variations in critical nucleotide sequences in evolution. *J. Mol. Evol.* **40,** 531–536
15. O'Donoghue, P., and Luthey-Schulten, Z. (2003) On the evolution of structure in aminoacyl-tRNA synthetases. *Microbiol. Mol. Biol. Rev.* **67,** 550–573
16. Cusack, S. (1995) Eleven down and nine to go. *Nat. Struct. Biol.* **2,** 824–831
17. Xie, W., Nangle, L. A., Zhang, W., Schimmel, P., and Yang, X. L. (2007) Long-range structural effects of a Charcot-Marie-Tooth disease-causing mutation in human glycyl-tRNA synthetase. *Proc. Natl. Acad. Sci. U.S.A.* **104,** 9976–9981
18. Wakasugi, K., and Schimmel, P. (1999) Two distinct cytokines released from a human aminoacyl-tRNA synthetase. *Science* **284,** 147–151
19. Antonellis, A., Ellsworth, R. E., Sambuughin, N., Puls, I., Abel, A., Lee-Lin, S. Q., Jordanova, A., Kremensky, I., Christodoulou, K., Middleton, L. T., Sivakumar, K., Ionasescu, V., Funalot, B., Vance, J. M., Goldfarb, L. G., Fischbeck, K. H., and Green, E. D. (2003) Glycyl tRNA synthetase mutations in Charcot-Marie-Tooth disease type 2D and distal spinal muscular atrophy type V. *Am. J. Hum. Genet.* **72,** 1293–1299
20. Zhu, X., Liu, Y., Yin, Y., Shao, A., Zhang, B., Kim, S., and Zhou, J. (2009) MSC p43 required for axonal development in motor neurons. *Proc. Natl. Acad. Sci. U.S.A.* **106,** 15944–15949
21. Yannay-Cohen, N., Carmi-Levy, I., Kay, G., Yang, C. M., Han, J. M., Kemeny, D. M., Kim, S., Nechushtan, H., and Razin, E. (2009) LysRS serves as a key signaling molecule in the immune response by regulating gene expression. *Mol. Cell* **34,** 603–611
22. Skre, H. (1974) Genetic and clinical aspects of Charcot-Marie-Tooth's disease. *Clin. Genet.* **6,** 98–118
23. Jani-Acsadi, A., Krajewski, K., and Shy, M. E. (2008) Charcot-Marie-Tooth neuropathies: diagnosis and management. *Semin. Neurol.* **28,** 185–194
24. Vallat, J. M., Mathis, S., and Funalot, B. (2013) The various Charcot-Marie-Tooth diseases. *Curr. Opin. Neurol.* **26,** 473–480
25. Thomas, P. K., and Calne, D. B. (1974) Motor nerve conduction velocity in peroneal muscular atrophy: evidence for genetic heterogeneity. *J. Neurol. Neurosurg. Psychiatry* **37,** 68–75
26. Bienfait, H. M., Baas, F., Koelman, J. H., de Haan, R. J., van Engelen, B. G., Gabreëls-Festen, A. A., Ongerboer de Visser, B. W., Meggouh, F., Weterman, M. A., De Jonghe, P., Timmerman, V., and de Visser, M. (2007) Phenotype of Charcot-Marie-Tooth disease type 2. *Neurology* **68,** 1658–1667
27. Saporta, M. A., and Shy, M. E. (2013) Inherited peripheral neuropathies. *Neurol. Clin.* **31,** 597–619
28. Barisic, N., Claeys, K. G., Sirotković-Skerlev, M., Löfgren, A., Nelis, E., De Jonghe, P., and Timmerman, V. (2008) Charcot-Marie-Tooth disease: a clinico-genetic confrontation. *Ann. Hum. Genet.* **72,** 416–441
29. Griffin, L. B., Sakaguchi, R., McGuigan, D., Gonzalez, M. A., Searby, C., Züchner, S., Hou, Y. M., and Antonellis, A. (2014) Impaired function is a common feature of neuropathy-associated glycyl-tRNA synthetase mutations. *Hum. Mutat.* **35,** 1363–1371
30. Motley, W. W., Talbot, K., and Fischbeck, K. H. (2010) *GARS* axonopathy: not every neuron's cup of tRNA. *Trends Neurosci.* **33,** 59–66
31. Lee, H. J., Park, J., Nakhro, K., Park, J. M., Hur, Y. M., Choi, B. O., and Chung, K. W. (2012) Two novel mutations of GARS in Korean families with distal hereditary motor neuropathy type V. *J. Peripher. Nerv. Syst.* **17,** 418–421
32. Yao, P., and Fox, P. L. (2013) Aminoacyl-tRNA synthetases in medicine and disease. *EMBO Mol. Med.* **5,** 332–343
33. Sivakumar, K., Kyriakides, T., Puls, I., Nicholson, G. A., Funalot, B., Antonellis, A., Sambuughin, N., Christodoulou, K., Beggs, J. L., Zamba-Papanicolaou, E., Ionasescu, V., Dalakas, M. C., Green, E. D., Fischbeck, K. H., and Goldfarb, L. G. (2005) Phenotypic spectrum of disorders associated with glycyl-tRNA synthetase mutations. *Brain* **128,** 2304–2314
34. Del Bo, R., Locatelli, F., Corti, S., Scarlato, M., Ghezzi, S., Prelle, A., Fagiolari, G., Moggio, M., Carpo, M., Bresolin, N., and Comi, G. P. (2006) Coexistence of CMT-2D and distal SMA-V phenotypes in an Italian family with a *GARS* gene mutation. *Neurology* **66,** 752–754
35. Seburn, K. L., Nangle, L. A., Cox, G. A., Schimmel, P., and Burgess, R. W. (2006) An active dominant mutation of glycyl-tRNA synthetase causes neuropathy in a Charcot-Marie-Tooth 2D mouse model. *Neuron* **51,** 715–726
36. James, P. A., Cader, M. Z., Muntoni, F., Childs, A. M., Crow, Y. J., and Talbot, K. (2006) Severe childhood SMA and axonal CMT due to anti-

codon binding domain mutations in the *GARS* gene. *Neurology* **67,** 1710–1712
37. Qin, X., Hao, Z., Tian, Q., Zhang, Z., Zhou, C., and Xie, W. (2014) Cocrystal structures of glycyl-tRNA synthetase in complex with tRNA suggest multiple conformational states in glycylation. *J. Biol. Chem.* **289,** 20359–20369
38. Logan, D. T., Mazauric, M. H., Kern, D., and Moras, D. (1995) Crystal structure of glycyl-tRNA synthetase from *Thermus thermophilus*. *EMBO J.* **14,** 4156–4167
39. McPherson, A., and Cudney, B. (2006) Searching for silver bullets: an alternative strategy for crystallizing macromolecules. *J. Struct. Biol.* **156,** 387–406
40. Otwinowski, Z., and Minor, W. (1997) Processing of x-ray diffraction data collected in oscillation mode. *Methods Enzymol.* **276,** 307–326
41. Adams, P. D., Afonine, P. V., Bunkóczi, G., Chen, V. B., Davis, I. W., Echols, N., Headd, J. J., Hung, L. W., Kapral, G. J., Grosse-Kunstleve, R. W., McCoy, A. J., Moriarty, N. W., Oeffner, R., Read, R. J., Richardson, D. C., Richardson, J. S., Terwilliger, T. C., and Zwart, P. H. (2010) Phenix: a comprehensive Python-based system for macromolecular structure solution. *Acta Crystallogr. D Biol. Crystallogr.* **66,** 213–221
42. Emsley, P., Lohkamp, B., Scott, W. G., and Cowtan, K. (2010) Features and development of Coot. *Acta Crystallogr. D Biol. Crystallogr.* **66,** 486–501
43. Afonine, P. V., Grosse-Kunstleve, R. W., Echols, N., Headd, J. J., Moriarty, N. W., Mustyakimov, M., Terwilliger, T. C., Urzhumtsev, A., Zwart, P. H., and Adams, P. D. (2012) Towards automated crystallographic structure refinement with phenix.refine. *Acta Crystallogr. D Biol. Crystallogr.* **68,** 352–367
44. Ren, J., Wen, L., Gao, X., Jin, C., Xue, Y., and Yao, X. (2009) DOG 1.0: illustrator of protein domain structures. *Cell Res* **19,** 271–273
45. Hess, B., Kutzner, C., van der Spoel, D., and Lindahl, E. (2008) GROMACS 4: algorithms for highly efficient, load-balanced, and scalable molecular simulation. *J. Chem. Theory Comput.* **4,** 435–447
46. MacKerell, A. D., Bashford, D., Bellott, M., Dunbrack, R. L., Evanseck, J. D., Field, M. J., Fischer, S., Gao, J., Guo, H., Ha, S., Joseph-McCarthy, D., Kuchnir, L., Kuczera, K., Lau, F. T., Mattos, C., *et al.* (1998) All-atom empirical potential for molecular modeling and dynamics studies of proteins. *J. Phys. Chem. B* **102,** 3586–3616
47. Jorgensen, W. L., Chandrasekhar, J., Madura, J. D., Impey, R. W., and Klein, M. L. (1983) Comparison of simple potential functions for simulating liquid water. *J. Chem. Physics* **79,** 926–935
48. Hockney, R., Goel, S., and Eastwood, J. (1974) Quiet high-resolution computer models of a plasma. *J. Comput. Physics* **14,** 148–158
49. Berendsen, H. J., Postma, J. P. M., van Gunsteren, W. F., DiNola, A., and Haak, J. (1984) Molecular dynamics with coupling to an external bath. *J. Chem. Physics* **81,** 3684–3690
50. Bussi, G., Donadio, D., and Parrinello, M. (2007) Canonical sampling through velocity rescaling. *J. Chem. Physics* **126,** 014101
51. Hess, B. (2008) P-LINCS: A parallel linear constraint solver for molecular simulation. *J. Chem. Theory Comput.* **4,** 116–122
52. Essmann, U., Perera, L., Berkowitz, M. L., Darden, T., Lee, H., and Pedersen, L. G. (1995) A smooth particle mesh Ewald method. *J. Chem. Physics* **103,** 8577–8593
53. Humphrey, W., Dalke, A., and Schulten, K. (1996) VMD: visual molecular dynamics. *J. Mol. Graphics* **14,** 33–38
54. Achilli, F., Bros-Facer, V., Williams, H. P., Banks, G. T., AlQatari, M., Chia, R., Tucci, V., Groves, M., Nickols, C. D., Seburn, K. L., Kendall, R., Cader, M. Z., Talbot, K., van Minnen, J., Burgess, R. W., Brandner, S., Martin, J. E., Koltzenburg, M., Greensmith, L., Nolan, P. M., and Fisher, E. M. (2009) An ENU-induced mutation in mouse glycyl-tRNA synthetase (GARS) causes peripheral sensory and motor phenotypes creating a model of Charcot-Marie-Tooth type 2D peripheral neuropathy. *Dis. Model Mech.* **2,** 359–373
55. Guo, R. T., Chong, Y. E., Guo, M., and Yang, X. L. (2009) Crystal structures and biochemical analyses suggest a unique mechanism and role for human glycyl-tRNA synthetase in Ap4A homeostasis. *J. Biol. Chem.* **284,** 28968–28976
56. Jordanova, A., Irobi, J., Thomas, F. P., Van Dijck, P., Meerschaert, K., Dewil, M., Dierick, I., Jacobs, A., De Vriendt, E., Guergueltcheva, V., Rao, C. V., Tournev, I., Gondim, F. A., D'Hooghe, M., Van Gerwen, V., Callaerts, P., Van Den Bosch, L., Timmermans, J. P., Robberecht, W., Gettemans, J., Thevelein, J. M., De Jonghe, P., Kremensky, I., and Timmerman, V. (2006) Disrupted function and axonal distribution of mutant tyrosyl-tRNA synthetase in dominant intermediate Charcot-Marie-Tooth neuropathy. *Nat. Genet.* **38,** 197–202
57. Désarnaud, F., Do Thi, A. N., Brown, A. M., Lemke, G., Suter, U., Baulieu, E. E., and Schumacher, M. (1998) Progesterone stimulates the activity of the promoters of peripheral myelin protein-22 and protein zero genes in Schwann cells. *J. Neurochem.* **71,** 1765–1768
58. Latour, P., Thauvin-Robinet, C., Baudelet-Méry, C., Soichot, P., Cusin, V., Faivre, L., Locatelli, M. C., Mayençon, M., Sarcey, A., Broussolle, E., Camu, W., David, A., and Rousson, R. (2010) A major determinant for binding and aminoacylation of tRNA(Ala) in cytoplasmic alanyl-tRNA synthetase is mutated in dominant axonal Charcot-Marie-Tooth disease. *Am. J. Hum. Genet.* **86,** 77–82
59. McLaughlin, H. M., Sakaguchi, R., Liu, C., Igarashi, T., Pehlivan, D., Chu, K., Iyer, R., Cruz, P., Cherukuri, P. F., Hansen, N. F., Mullikin, J. C., NISC Comparative Sequencing Program, Biesecker, L. G., Wilson, T. E., Ionasescu, V., Nicholson, G., Searby, C., Talbot, K., Vance, J. M., Züchner, S., Szigeti, K., Lupski, J. R., Hou, Y. M., Green, E. D., and Antonellis, A. (2010) Compound heterozygosity for loss-of-function lysyl-tRNA synthetase mutations in a patient with peripheral neuropathy. *Am. J. Hum. Genet.* **87,** 560–566
60. Shi, Y., Xu, X., Zhang, Q., Fu, G., Mo, Z., Wang, G. S., Kishi, S., and Yang, X. L. (2014) tRNA synthetase counteracts c-Myc to develop functional vasculature. *eLife* **3,** e02349

Large Conformational Changes of Insertion 3 in Human Glycyl-tRNA Synthetase (hGlyRS) during Catalysis

Xiangyu Deng, Xiangjing Qin, Lei Chen, Qian Jia, Yonghui Zhang, Zhiyong Zhang, Dongsheng Lei, Gang Ren, Zhihong Zhou, Zhong Wang, Qing Li and Wei Xie

J. Biol. Chem. 2016, 291:5740-5752.
doi: 10.1074/jbc.M115.679126 originally published online January 21, 2016